ACS APPLIED MATERIALS & INTERFACES

Research Article

Cite This: ACS Appl. Mater. Interfaces 2019, 11, 11431−11441

www.acsami.org

Carbon Nitride Phosphorus as an Effective Lithium Polysulfide Adsorbent for Lithium−Sulfur Batteries

Vandung Do,[†,‡] Deepika,[§] Mun Sek Kim,[†] Min Seop Kim,[†,∥] Kwang Ryeol Lee,*[,§] and Won Il Cho*[,†]

[†]Center for Energy Storage Research and [§]Computational Science Research Center, Korea Institute of Science and Technology, Seoul 02792, Republic of Korea

[‡]Division of Energy and Environmental Technology, Korea University of Science and Technology (UST), Daejeon 34113, Republic of Korea

[∥]Department of Materials Science and Engineering, Korea University, Seoul 02841, Republic of Korea

Supporting Information

ABSTRACT: Lithium−sulfur (Li−S) batteries are attracting substantial attention because of their high-energy densities and potential applications in portable electronics. However, an intrinsic property of Li−S systems, that is, the solubility of lithium polysulfides (LiPSs), hinders the commercialization of Li−S batteries. Herein, a new material, that is, carbon nitride phosphorus (CNP), is designed and synthesized as a superior LiPS adsorbent to overcome the issues of Li−S batteries. Both the experimental results and the density functional theory (DFT) calculations confirm that CNP possesses the highest binding energy with LiPS at a P concentration of ∼22% (CNP22). The DFT calculations explain the simultaneous existence of Li−N bonding and P−S coordination in the sulfur cathode when CNP22 interacts with LiPS. By introducing CNP22 into the Li−S systems, a sufficient charging capacity at a low cutoff voltage, that is, 2.45 V, is effectively implemented, to minimize the side reactions, and therefore, to prolong the cycling life of Li−S systems. After 700 cycles, a Li−S cell with CNP22 gives a high discharge capacity of 850 mA h g^{-1} and a cycling stability with a decay rate of 0.041% $cycle^{-1}$. The incorporation of CNP22 can achieve high performance in Li−S batteries without concerns regarding the LiPS shuttling phenomenon.

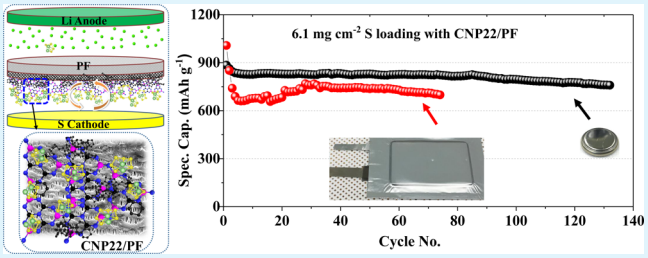

KEYWORDS: *carbon nitride phosphorus, lithium−sulfur batteries, adsorbent, lithium polysulfides, shuttling phenomenon, P−S bond, DFT calculation*

1. INTRODUCTION

The rapid development of modern society and the electronic and automobile industries have led to the need for electrochemical-energy-storage systems (ESSs) that eliminate the problem of smog related to internal combustion engine and their release of NO_x, SO_x, CO_2, and other particulates. There is also a need to develop advanced rechargeable batteries with excellent properties, for example, a high capacity, a low weight, a low cost, and a high level of safety, to satisfy the ever-increasing energy demand for ESSs. Among various rechargeable systems, lithium-ion batteries (LiBs) address the need for ESSs and have become prominent in portable electronics and stationary applications. However, statistics about battery technology growth to date show that conventional LiB systems are reaching their theoretical limits, are expensive to produce, and have some safety issues.[1,2] Until now, Li−S batteries have been considered as the potential candidate for next-generation ESSs because of their high theoretical capacity and energy density, that is, up to 1673 mA h g^{-1} and 2600 W h kg^{-1}, respectively.[3,4] Despite these advantages, some technical problems associated with both Li anodes and S cathodes remain and hinder the wide commercialization of Li−S batteries. The obstacles related to the anode include Li nucleation and sharp dendritic growth during battery cycling.[5−9] On the cathode side, the shuttle phenomenon, natural insulating properties of S, and volume expansion of the S cathode (∼80%) are major problems that cause significant capacity fading in Li−S batteries.[10−12] Recently, the construction of an artificial solid−electrolyte interphase layer on the refined Li metal surface[13−15] and the use of Al_2O_3/graphite as an anode surface passivation layer to maintain a thin and stable SEI layer and to mitigate the shuttle effect have been recorded.[16] Some research groups have discovered that the self-healing of the Li surface by a high current density treatment can significantly suppress the Li dendritic growth[17] or the parasitic reaction of LiPS with the Li anode.[18] Noticeable improvements in the S cathode performance have been achieved by various techniques. For example, some studies have reported that the electrochemical performance of Li−S batteries is enhanced by a porous C interlayer between

Received: December 20, 2018
Accepted: March 7, 2019
Published: March 7, 2019

DOI: 10.1021/acsami.8b22249
ACS Appl. Mater. Interfaces 2019, 11, 11431−11441

the S cathode and a polyolefin film (PF).[19−21] In addition, free-standing carbon nanofiber and carbon paper have also been investigated as efficient interlayers that are highly effective in limiting the shuttling phenomenon and acting as the second current collector, thereby greatly increasing the cell performance.[22,23] However, unfavorable interactions between nonpolar C and polar soluble LiPS are the main cause of the inability of the interlayer to maintain battery performance. Other studies have focused on the use of PF modified by metal compound (TiO_2, InN, SnS_2, $FeCo_2S_4$, $Co(OH)_2$, Fe_3O_4, and MoO_3@CNT) as cathode frameworks because of their natural polarization properties, which enable good adsorption of LiPS.[24−30] Despite good LiPS adsorption, two key factors, that is, low conductivities and high densities, of such metal compound simultaneously decrease the energy density of Li−S battery systems. In other cases, C surfaces have been modified by N doping to increase the LiPS adsorption capability, while retaining the electrical conductivity. However, the LiPS adsorption of these materials is finite and can be attributed to the low doping concentration.[31,32]

Recently, the conventional carbon nitride (CNP0) has generally been applied in Li−S batteries as a supporting material to capture LiPS. However, the electrochemical performance has been achieved at low S loading (0.85−2.3 mg cm^{-2}).[33−37] Weak LiPS adsorption and the very poor electrical conductivity of carbon nitride are considered to be the main causes limiting the effectiveness of this material. To bypass these issues in Li−S batteries, a new material needs to be developed and applied not only for the stability of Li−S batteries but also for the application of high-S-loaded cathodes. Herein, carbon nitride phosphorus (CNP) is designed and synthesized by the simultaneous pyrolysis of urea and diammonium phosphate for applications in the cathode side of Li−S batteries. CNP exhibits strong LiPS adsorption and possesses a higher electrical conductivity[38] than CNP0. Density functional theory (DFT) calculations show that there is a critical level of substitution of C by P atoms, which results in an increase in the electrical conductivity and the binding strength between LiPS and the CNP substrate. Two different mechanisms of LiPS adsorption on CNP-coated PF and pristine PF are proposed, as shown in Scheme 1. The analysis of the projected density of states (PDOSs), charge density differences, and Bader charge further shows that in addition to electrostatic interactions between Li and N atoms, P forms covalent bonds with S (P−S coordination), which enhances the binding strength of LiPS molecules with the CNP substrate. CNP, therefore, gives not only pyridinic N but also generates additional P binding sites for superior LiPS adsorption.

2. EXPERIMENTAL SECTION

2.1. CNP Synthesis. Herein, polar CNP materials were synthesized by simple pyrolysis of urea ($(NH_2)_2CO$) and diammonium phosphate ($(NH_4)_2HPO_4$), as shown in Figure S1. In detail, a mixture of $(NH_2)_2CO$ and $(NH_4)_2HPO_4$ was placed in a crucible, which was then sealed with an aluminum foil and a cover on top. The pyrolysis was performed at 550 °C for 2 h in a box furnace in air at a ramp rate of 5 °C min^{-1} (Figure S1a). The amount of $(NH_4)_2HPO_4$ was varied to change the P concentration in the CNP samples, that is, CNPx (x = 0, 7.2, 14, 22, 29, and 36) corresponding to P concentrations in CNP of 0, 7.2, 14, 22, 29, and 36%, respectively, as shown in Figure S2a. The average particle sizes of CNP0 and CNP22 are smaller than 200 nm as seen from scanning electron microscopy (SEM) images (Figure S1b,c). The obtained

Scheme 1. Schematic Model Compares the Different Mechanisms of LiPS Adsorption between CNP22/PF (Left) and Pristine PF (Right) in the Li−S Batteries

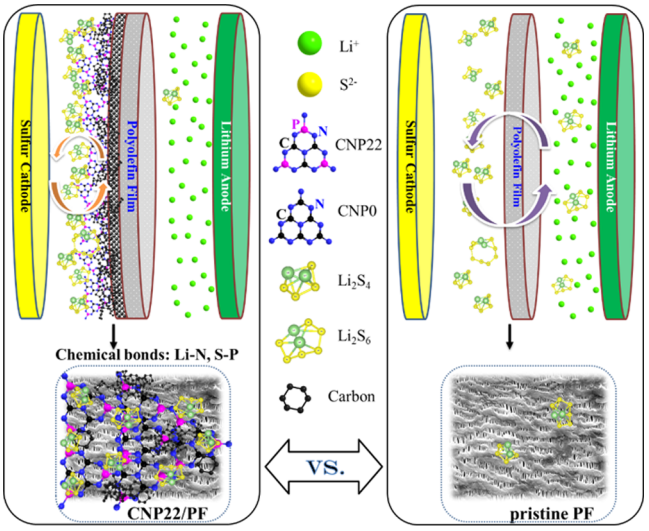

yield of CNP22 is substantially higher (16.8%) than that of CNP0 (3.6%) (see analysis in the Supporting Information and Figure S5). After pyrolysis, the CNP samples were ground, ultrasonicated, and then washed three times with deionized water and ethanol before drying at 80 °C in a vacuum oven for 24 h to obtain the final products. The surface area of CNP0 (22 m^2 g^{-1}) and CNP22 (16 m^2 g^{-1}) and the pore size distributions were confirmed by the Brunauer−Emmett−Teller and Barrett−Joyner−Halenda methods (Figure S2b,c).

2.2. CNP-Coated PF Fabrication. PF modification is one of the most effective methods to achieve high efficiency and to minimize the shuttle phenomenon in Li−S batteries.[17] Therefore, CNP22 was coated uniformly on the PF (CNP22/PF) to capture and reutilize LiPS efficiently. The CNP22/PF was fabricated by coating a slurry comprising CNP22, super P carbon (TIMCAL), vapor-grown carbon fiber, and polyvinylidene fluoride binder (a ratio of 7:1:1:1) on the commercial PF (Celgard 2500). The density of the coated layer was ca. 0.7 mg cm^{-2}. Figure S4a shows digital photographs of CNP22/PF as casted and after drying. The thickness of the coated layer was also investigated by a 3D laser microscope, as seen in Figure S4b. To optimize the P concentration in CNP, other samples such as CNP0, CNP7.2, CNP14, CNP29, and CNP36 coated-PF were also prepared.

3. RESULTS AND DISCUSSION

3.1. Structural Analysis of CNP. CNPx was simply synthesized and produced with a high yield as noted in the Experimental Section and Figures S1 and S2. The morphologies of CNP0 and CNP22 were investigated by scanning transmission electron microscopy, which show nanoporous structures and uniform distributions of C, N, and O for CNP0 (Figure S3a) and C, N, O, and P for CNP22 (Figure S3b,c). X-ray diffraction (XRD) was used to investigate the crystal structures of CNP0, CNP7.2, CNP14, and CNP22, which correspond to P concentrations of 0, 7.2, 14, and 22%, respectively (Figure 1a). The XRD pattern of CNP0 shows two peaks, at 13.1° and 27.3°, corresponding to the (100) and (002) planes, respectively. Interestingly, the peak intensities decrease with increasing content of P in CNP, and no peak is observed for CNP22. In addition, high-resolution TEM images (Figure 1b,c) and their corresponding selected-area electron diffraction (SAED) patterns (Figure 1d,e) confirm the crystallographic structures of CNP0 and CNP22. The CNP0-

DOI: 10.1021/acsami.8b22249
ACS Appl. Mater. Interfaces 2019, 11, 11431−11441

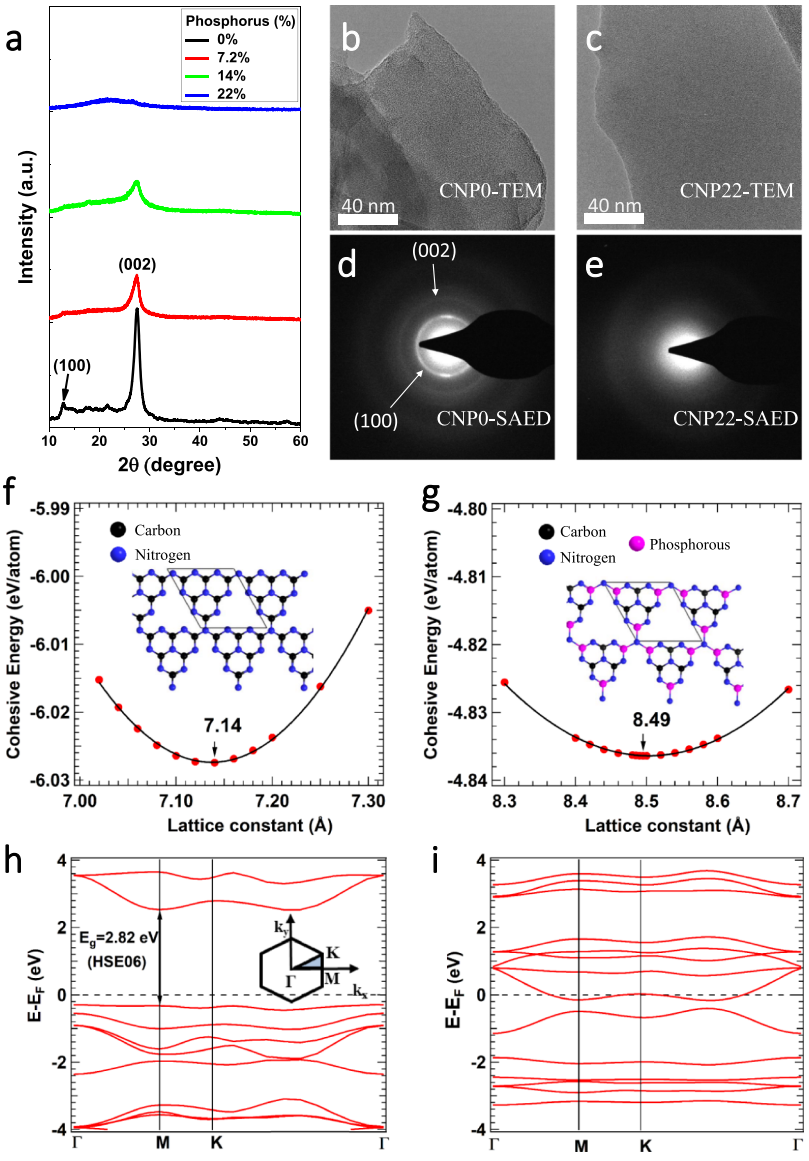

Figure 1. Structural analysis of CNP. (a) XRD patterns of CNP0, CNP7.2, CNP14, and CNP22; (b,d) high-resolution TEM images and SAED patterns for CNP0; (c,e) high-resolution TEM images and SAED patterns for CNP22. The images show that CNP0 has a crystalline phase, whereas CNP22 is a mainly amorphous material. (f,g) Lattice constants of CNP0 and CNP22, respectively; the atomic bonding structures in insets in part (f,g) are used for DFT calculation, with black, blue, and pink spheres represent C, N, and P atoms, respectively. (h,i) Corresponding electron band gap structures obtained by using hybrid GGA and the SE06 functional, for CNP0 and CNP22, respectively.

SAED pattern shows two diffraction rings, that is, inner (bright) and outer (dim) rings, corresponding to the (100) and (002) planes (Figure 1d). No diffraction ring is observed in the CNP22-SAED pattern (Figure 1e). These results are in agreement with the XRD patterns, which confirm that the crystallinity of CNP0 differs from that of CNP22 and that the CNP structure varies according to the P content. The atomic bonding structure of CNP22 is assumed as shown in the inset in Figure 1g, based on the following proofs. First, to incorporate the P atoms in the atomic structure of CNP0, the DFT calculations were performed for both interstitial and substitutional doping P, which shows the substitutional doping P in CNP0 offering the minimum energy configurations. In all cases of substituting P to C or N, only the substitution of the edge C (C_1 positions in the inset in Figure S14a) that creating the bond of two heptazine rings will create a symmetrical and stable atomic structure. Further, the experimental study performed by Zhang et al. confirmed that P doping in CNP0 leads to the replacement only of the C atoms.[39] Second, the energy-dispersive X-ray spectroscopy results of various concentrations of P in CNP (Figure S13) show that the P peak intensity clearly increases with decreasing C peak intensity (when compared to the N peak) from CNP0 to CNP36. This finding suggests that the P substituent occurs only at the edge C atoms. Third, the study of binding energy (BE) by the X-ray photoelectron spectroscopy (XPS) measurement conducted on CNP22 powder (as discussed below) shows that only bonding between P and N exists. Similarly, no bonding between P and C is observed in the deconvolution of the C 1s XPS spectra of CNP0 and CNP22 powders (Figure S9e). These arguments reinforce the accuracy of the atomic bonding structure of CNP22 presented in this study.

DOI: 10.1021/acsami.8b22249
ACS Appl. Mater. Interfaces 2019, 11, 11431−11441

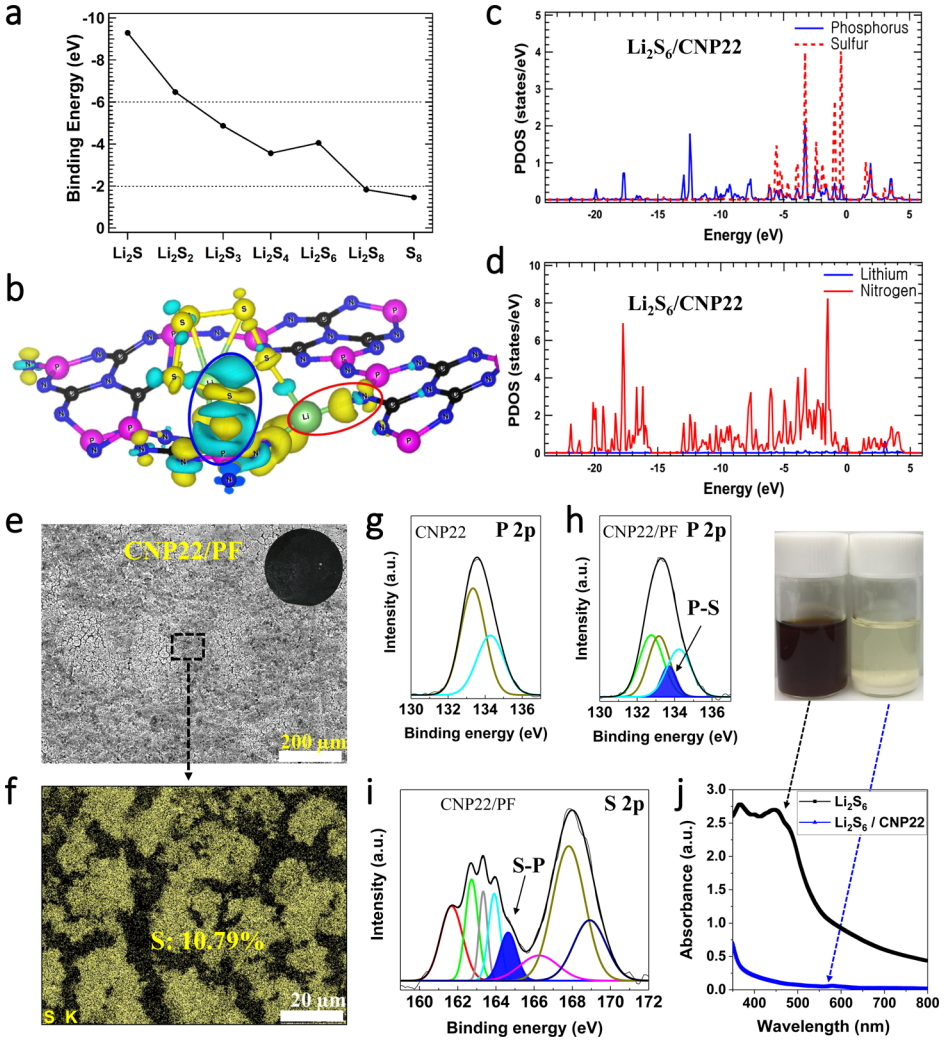

Figure 2. Analysis of binding energies between CNP22 and LiPS. (a) Plot of binding energies of various LiPSs on CNP22. (b) Schematic diagram of the charge density difference after adsorption of Li_2S_6 on CNP22. Yellow, green, black, blue, and pink spheres represent S, Li, C, N, and P atoms, respectively. Charge accumulations and depletion are shown in dark yellow and aqua blue color, respectively. The red circle shows the Li−N bond, and the blue circle shows the P−S bond. (c,d) PDOS for Li_2S_6 adsorbed on the CNP22 substrate: (c) Orbitals around Fermi level for P and S show the P−S covalent bond, and (d) orbitals around Fermi level for Li and N show the Li−N electrostatic bond. (e) SEM image and (f) S elemental mapping for CNP22/PF after 100 cycles. The inset in part 2e shows a digital photograph of CNP22/PF after disassembling Li−S cell. (g,h) P 2p scanning XP spectra for CNP22 powder and CNP22/PF, respectively. (i) S 2p scanning XP spectra for CNP22/PF. (j) UV−vis absorption spectrum of the electrolyte solution (diluted 10 times before measurement) without and with CNP22; the mid-right inset shows photograph of original vials containing the electrolyte solutions without and with CNP22.

The DFT calculations were performed on the atomic bonding structures (insets in Figure 1f,g) by the Vienna Ab initio Simulation Package,[40] which shows that the lattice parameter increases from 7.14 Å in CNP0 (Figure 1f) to 8.49 Å in CNP22 (Figure 1g). The intervention of a sufficiently high amount of P atoms in the phase formation of CNP results into a gradual phase shift from the crystalline phase (of CNP0) to amorphous phase (of CNP22). The increase in the lattice parameter and degree of atomic disorder in CNP22 can enlarge the volume and external pressure (see Table S1) on the optimized unit cell with a gradual increase in the P-substitution, which distorts the periodicity of CNP22, whereas CNP0 maintains the periodicity, as shown in Figure 1f. The increase in the volume of the unit cell of CNP22 is due to the large atomic radii of P than C, which sources the increase in external pressure on the unit cell. The energetically stable geometry of the CNP22 at absolutely zero external pressure can be retained only with an increase in the lattice constant of the CNP22 from 7.14 to 8.49 Å (Figure 1g). Therefore, the amorphous phase of CNP22 can be explained by the loss in the periodicity of the CNP22 at smaller lattice constant value of CNP0 (7.14 Å). For the band structure, the theoretical band gap of CNP0 is calculated to be ca. 2.82 eV (Figure 1h), which is consistent with previously reported experimental band gap values.[41,42] Contrarily, the band gap of CNP22 narrows significantly, which indicates that it may have a better conductivity than CNP0 (Figure 1i). It is observed that the band gap of an amorphous semiconducting material is smaller than that of the corresponding crystalline material because of the presence of band tails.[43] This result confirms that the change in the crystallinity of CNP0 to the amorphous state caused by substitution with 22% P could decrease the band gap and increase the electrical conductivity of the CNP22 material. The transition to the amorphous phase and decrease in the band gap of CNP22 are very important premises for the selection of a supporting material in Li−S systems.

DOI: 10.1021/acsami.8b22249
ACS Appl. Mater. Interfaces 2019, 11, 11431−11441

3.2. Binding Energies of CNP22 and LiPS. Once the above CNP structures were investigated and optimized, the LiPS adsorption by CNP was studied and verified theoretically and experimentally. The redox species of Li and S (Li_2S_x, x = 1, 2, 3, 4, 6, and 8) and their optimized structures are shown in Figure S6, where the Li−S bond lengths are shown to be in agreement with previous studies.[44] The effects of various adsorbed LiPS on CNP22 were examined by performing BE calculations, as shown in Figure 2a. Clearly, all of the soluble LiPS molecules present BE values in the approximate range of −2 to −6 eV, corresponding to attractive interactions, which explains the good LiPS adsorption capability of CNP22. Moreover, the interaction of Li_2S_6 on the CNP22 supercell was proposed by DFT calculation to predict the LiPS adsorption intensity of the CNP22. Compared to the structure before relaxation (Figure S7a), a buckling of ca. 2.48 Å is observed after relaxation (Figure S7b), which indicates the deformation of the CNP22 substrate by a strong interaction with the LiPS. The BE values for Li_2S with various substrates were also calculated using DFT and are listed in Table 1. The highest

Table 1. Binding Energies of Li_2S with Various Substrates

substrate	pristine PF	CNP0	CNP7.2	CNP14	CNP22
BE of Li_2S (eV)	−1.27	−4.39	−5.15	−7.53	−9.28

binding strength, that is, −9.28 eV, is achieved with CNP22, whereas this value with pristine PF is very small, that is, −1.27 eV which confirms that the critical P concentration of 22% is the most suitable candidate for use in Li−S systems.

The differences in the typical charge densities were analyzed to visualize the adsorption interactions between LiPS and CNP22, as shown in Figure 2b. The charge cloud is shared equally between P and S because of their similar electronegativities,[45] whereas the accumulation of a charge cloud near N (yellow region) and change depletion near Li (blue region) results in ionic interactions between Li and N atoms.[33] The PDOSs were also analyzed to determine the types of interactions between Li_2S_6 and CNP22. Significant overlapping of the orbitals of P atoms with those of S around the Fermi level confirms covalent bonding between P and S atoms (Figure 2c). In contrast, the almost negligible overlapping of the orbitals of Li and N atoms indicates ionic interactions (Figure 2d). The P atoms in CNP22, therefore, interact covalently with the S atoms, whereas the N in CNP22 interacts electrostatically with Li from LiPS. Additionally, a Bader charge analysis was conducted to quantitatively determine the flow of charge transfer between the LiPS and CNP22 (Table S2). For the adsorption of a Li_2S molecule on CNP22, the Coulombic charges on Li before and after adsorption are estimated to be ca. 0.86e and 0.56e, respectively, suggesting that Li partially transfers its charge to N. Similarly, the Coulombic charge on S changes from ca. −1.72e before adsorption to −0.54e after adsorption, indicating charge transfer from Li_2S to CNP22. The charge transfers for other LiPS are listed in Table S2. These results show that the charge is directly transferred from LiPS species to CNP22 in the Li−S systems.

To confirm our theoretical findings and to assess the efficacy of CNP22, the following cell configurations were used to clearly compare the utility of CNP22 and the electrochemical performances of Li−S cells, that is, Li|CNP22/PF|S and Li| CNP0/PF|S, with Li as the anode, modified PF, and S cathode. Figure S8 shows the surface morphologies of the cathodes with CNP22 and CNP0 after 100 cycles. The surface of the cathode in the Li|CNP22/PF|S cell (Figure S8a) remains more stable than the surface of the cathode in the Li|CNP0/PF|S cell (Figure S8b), which can be explained, based on the DFT calculations, as the deformation and relaxation of CNP22 during charge interactions with LiPS (Figure S7). It is conceivable that CNP22 stabilized S migration and helped to maintain the cathode's integrity during repeated volume changes with cycling. SEM (Figure 2e) and S-elemental mapping (Figure 2f) were performed on CNP22/PF to investigate the LiPS adsorption capabilities of CNP22. The results show that ca. 10.79% of S is captured on CNP22/PF, which is higher than ca. 2.84% on CNP0/PF (Figure S8c), indicating that CNP22 provides far better LiPS adsorption. The chemical interactions with LiPS were clarified by XPS of the surface of CNP22/PF after the 100th cycle and on pristine CNP22 powder. The XPS spectrum of CNP22/PF contains two peaks, at 133 and 189 eV, which do not appear in the CNP0/PF spectrum. These new peaks are assigned to P 2p and P 2s bonds, as seen in Figure S9a. The P 2p spectrum of the CNP22 powder (Figure 2g) shows two peaks, at 133.3 and 134.3 eV, corresponding to P−N[38] and C−O−PO_3 bonds.[46] The P 2p spectrum of CNP22/PF after cycling in the Li−S cell (Figure 2h) was deconvoluted into four P components, of which two counterparts belong to the intrinsic P−N and C−O−PO_3 bonds, whereas the peaks at 132.7 and 133.7 eV can be ascribed to P−C[46] and P−S bonds, respectively. The P−C bond in this case refers to the bond between the P of CNP22 and the C of the conducting agent. For the S peaks, the spectra of S 2p in CNP22/PF (Figure 2i) and CNP0/PF (Figure S9b) show coincidence at low-energy bands such as 161.5, 162.7, 163.3, and 163.9 eV, which corresponds to the terminal S, C−S, bridging S, and central S polysulfide bonds, respectively.[47−49] Notably, we observe a peak at 164.6 eV in the S 2p spectrum of only CNP22/PF. Our DFT calculations suggest that the peak at 164.6 eV can be attributed to the S−P bond. Another study has confirmed that S with this peak position tends to act as an electron donor,[50] which agrees well with our DFT calculations.

In addition to the chemical interactions assessed above, LiPS adsorption on CNP0 and CNP22 was also visualized by conducting adsorption experiments (the color change of Li_2S_6 and Li_2S_4 solutions), as shown in Figure S10. It can be seen that 0.2 mmol Li_2S_6 in the electrolyte solution is partially and completely adsorbed by 50 mg of CNP22 after 15 and 45 min. In contrast, a negligible color change is observed for the vial containing CNP0 after 45 min. These results show that CNP22 adsorbs a significant amount of Li_2S_6 (Figure S10a) and Li_2S_4 (Figure S10b) and distinctly changes the color of the concentrated LiPS solution. The adsorption capacity of CNP22 was further investigated by adding additional Li_2S_6 as seen in Figure S11. After 90 min, 50 mg of CNP22 effectively adsorbs more than 0.3 mmol Li_2S_6, which indicates the strong LiPS adsorptivity of CNP22. Furthermore, to measure the characteristic adsorption spectrum of Li_2S_6 and to obtain a scientific view of Li_2S_6 adsorption of CNP22, the solvents in the color change test (shown in Figure S10) were measured with UV−vis spectroscopy. The blue line in Figure 2j depicts a very low intensity of spectrum, which means that no Li_2S_6 remains in the electrolyte solution, implying that CNP22 adsorbed all Li_2S_6.

DOI: 10.1021/acsami.8b22249
ACS Appl. Mater. Interfaces 2019, 11, 11431−11441

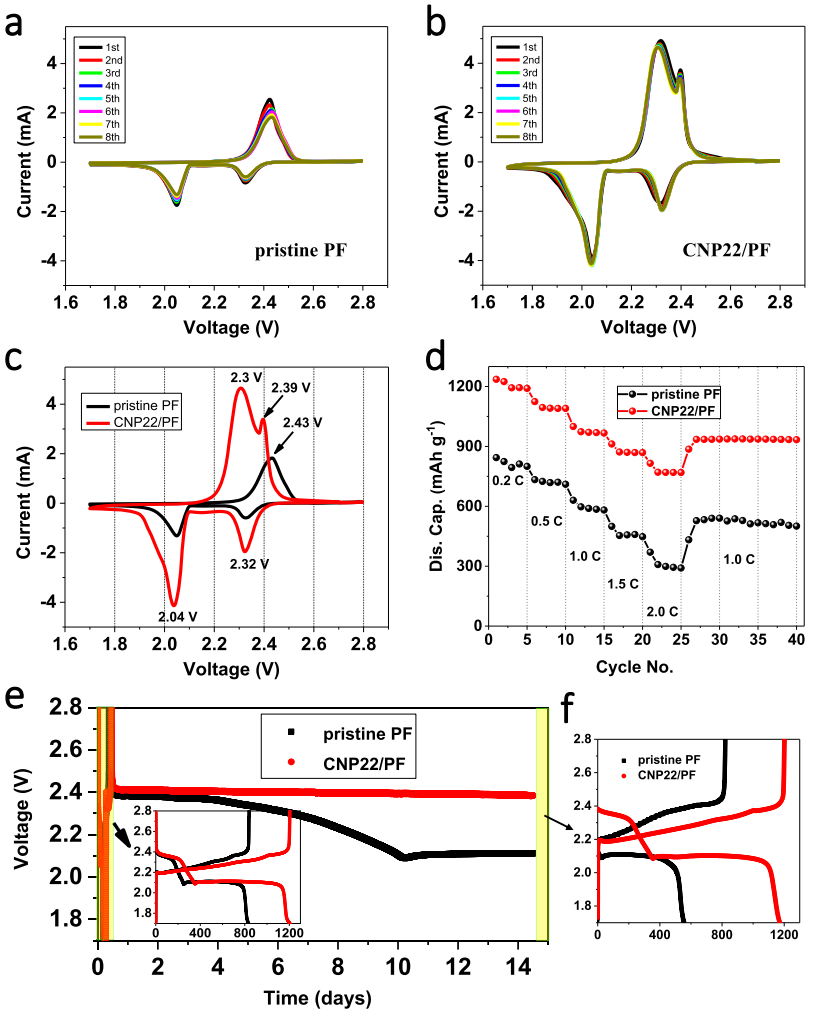

Figure 3. Electrochemical properties of the Li|CNP22/PF|S cell. (a,b) CV data for Li−S cells with pristine PF and CNP22/PF, respectively. (c) Comparison of the 8th cycles in CV curves (scanning rate 0.05 mV s^{-1}) and (d) rate performance of Li|PF|S and Li|CNP22/PF|S cells. (e) Self-discharge of Li|PF|S and Li|CNP22/PF|S cells after one cycle. The inset shows the charge/discharge curves for the first cycle at 0.2 C. (f) Charge/discharge curves at 0.2 C after 14 days of the self-discharge monitoring of the two Li−S cells.

3.3. Electrochemical Properties of the Li|CNP22/PF|S Cell Configuration. A deeper analysis of the electrochemical behavior of Li−S cells was performed to theoretically and experimentally verify the good LiPS adsorption of CNP22 (Figure 3). Cyclic voltammograms of Li−S cells with pristine PF or Li|PF|S and Li|CNP22/PF|S are shown and compared over eight cycles at 0.05 mV s^{-1} (Figure 3c). The peak intensities in the cyclic voltammograms of the Li|PF|S cell (Figure 3a) are relatively weak because of the low S utilization. Whereas more intense peaks are observed with the Li|CNP22/PF|S cell (Figure 3b), indicating high S utilization. Additionally, the difference between the positions of the cathodic peaks at 2.32 and 2.04 V (Figure 3c), which correspond to the conversion or reduction of S_8, respectively, is insignificant.[51] This finding suggests that CNP22 imparts no adverse effects to the electrochemical performance of the Li−S cell. In the anodic sweep, the difference between the peak positions of the Li|CNP22/PF|S cell is more pronounced and with a shift toward lower voltages that represents a reduction in the electrode polarization, which could significantly prolong the cell cycling life.[52] In addition, two separated peaks are observed at 2.3 and 2.39 V for the Li|CNP22/PF|S cell, which are indistinguishable for the case of the Li|PF|S cell, and indicate the stable and complete electrochemical conversion from the short-chain polysulfides to S. In detail, the peak at 2.3 V corresponds to the oxidation of short-chain polysulfides (Li_2S/Li_2S_2) to Li_2S_4, and the peak at 2.39 V corresponds to the oxidation to the long-chain polysulfides and S.[22,53] The complete conversion shown in the charging process means that CNP22 acts as a strong electrochemical catalyst, which helps to maintain the high performance of the discharge process.

Furthermore, the rate capability in Figure 3d reveals the significantly high performance of the Li|CNP22/PF|S cell compared to that of the Li|PF|S cell, tolerating 0.2−1.0 C. Percentage capacity changes of 8.6% (to 0.5 C), 8.2% (to 1 C), 11.5% (to 1.5 C), and 11.4% (to 2 C) are observed, and 78.4% of the capacity is retained at 1 C after cycling at various C rates. The enhanced rate capability can only be explained by the good LiPS adsorption to and desorption from CNP22, which contributes greatly to the alleviation of LiPS shuttling and the retention of the electrochemical reversibility. In another aspect, experimenting with Li−S batteries shows that they seriously suffer from self-discharge, which is mainly caused by the shuttling of LiPS.[54] This phenomenon leads to a low shelf-life, which impedes the commercialization of Li−S

DOI: 10.1021/acsami.8b22249
ACS Appl. Mater. Interfaces 2019, 11, 11431−11441

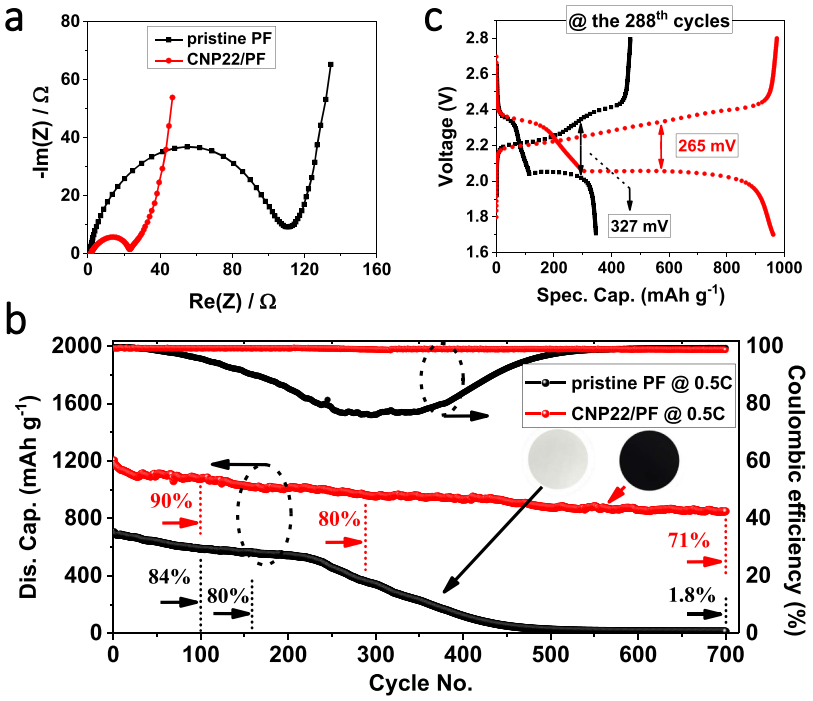

Figure 4. Electrochemical performance of the Li|CNP22/PF|S cell. Comparison on electrochemical properties of the Li|PF|S and Li|CNP22/PF|S cells, with a sulfur loading of 3.2 mg cm^{-2}: (a) electrospray-ionization spectroscopy results and (b) electrochemical performances in long-term cycling. The inset shows digital photographs of pristine PF (left) and CNP22/PF (right) before cell assembly. (c) Galvanostatic charge/discharge voltage profiles at the 288th cycles.

batteries. The self-discharge processes for Li|CNP22/PF|S and Li|PF|S cells were gathered by recording the open-circuit voltages over 14 days after both cells had undergone one full cycle at 0.2 C (Figure 3e). The voltage of the Li|PF|S cell decreases rapidly to 2.11 V (a decline of ∼11.7%) over 10 days, whereas the Li|CNP22/PF|S cell retained a voltage of 2.38 V (a decrease of ∼1.65%) after 14 days. Then, both cells were tested for their electrochemical performance to assess more detail about their capacity maintenance (as shown in Figure 3f). The second cycle shows that the Li|PF|S cell maintains 67% (556 mA h g^{-1}) capacity after the self-discharge monitoring process, which is a significant loss of capacity when compared to that of the Li|CNP22/PF|S cell (loss ≈ 2.4%). This difference in self-discharge is a clear evidence of the good LiPS adsorption properties of CNP22 that help to suppress spontaneous reactions between Li and S. This property plays an important role in stabilizing the electrochemical processes in Li−S systems, which are crucial for constructing reliable and practical Li−S batteries.

3.4. Electrochemical Performance of Li|CNP22/PF|S Cells. The above analysis focuses on the electrochemical properties of the Li|CNP22/PF|S cell, which partially confirms the overall electrochemical performance of Li−S cell; however, the electrochemical stability of a full cell configuration for a long period needs to be further investigated. It should be noted that in the design of cell components with added inactive materials, the effects of the inactive materials on the volumetric and gravimetric energy densities should be carefully assessed. The appropriate thickness and areal loading of the carbon-mixed CNP22 were designed to be 21 μm (Figure S4b) and 0.7 mg cm^{-2}, respectively; these values correspond to 9.3% of the overall thickness and 2.74% of the mass, as based on all of the cell components. Although introducing inactive materials into cell systems may lower the energy density, we later show that the actual increase in the electrochemical performance achieved by adding CNP22 more than that compensates for the energy reduction caused by the inert CNP22. This improvement is possible because S use does not usually reach 100% (1673 mA h g^{-1}), for all S cathodes.

On the basis of the electrochemical impedance spectroscopy obtained before cycling, the charge-transfer resistances are estimated to be 22 and 110 Ω cm^2 for the Li|PF|S and Li|CNP22/PF|S cells, respectively (Figure 4a). The impact of the CNP22/PF layer may be considered as the key for the decrease in impedance, and it is a starting point to explaining the high-cycling performance of the Li|CNP22/PF|S cell over 700 cycles, as shown in Figure 4b. In detail, the Li|PF|S cell (at 0.5 C) shows a rapid decay in discharge capacity from 704 (42% use of S) to 589 mA h g^{-1} (84% capacity retention) after 100 cycles that indicates a significant loss of active material. Under equivalent cycling conditions, the discharge capacity of the Li|CNP22/PF|S cell decreases from 1204 mA h g^{-1} (72% use of S) to 1079 mA h g^{-1} (90% capacity retention), that is, a significant improvement in the electrochemical performance is achieved. A comparison of the energy densities of two Li−S cell configurations shows that the volumetric and gravimetric energy densities increased by approximately 49.1% (see Table S3) and 49.6% (see Table S4), respectively, with an apparent increase in the cycling life (from 159 to 288 cycles, based on the cycles that gave 80% of the initial capacity). Over 700 cycles, a capacity retention of 1.8% (capacity of 12.6 mA h g^{-1}) is obtained for the Li|PF|S cell; this value is significantly lower than 71% (capacity of 850 mA h g^{-1}) of the Li|CNP22/PF|S cell. Furthermore, the decay rate calculation of the Li|CNP22/PF|S cell is only 0.041% $cycle^{-1}$, which is significantly lower than 0.14% of the Li|PF|S cell. After 288 cycles, a Coulombic efficiency (CE) of 99% is achieved for the Li|CNP22/PF|S cell, substantially higher than 77% of the Li|PF|S cell, indicating that

DOI: 10.1021/acsami.8b22249
ACS Appl. Mater. Interfaces 2019, 11, 11431−11441

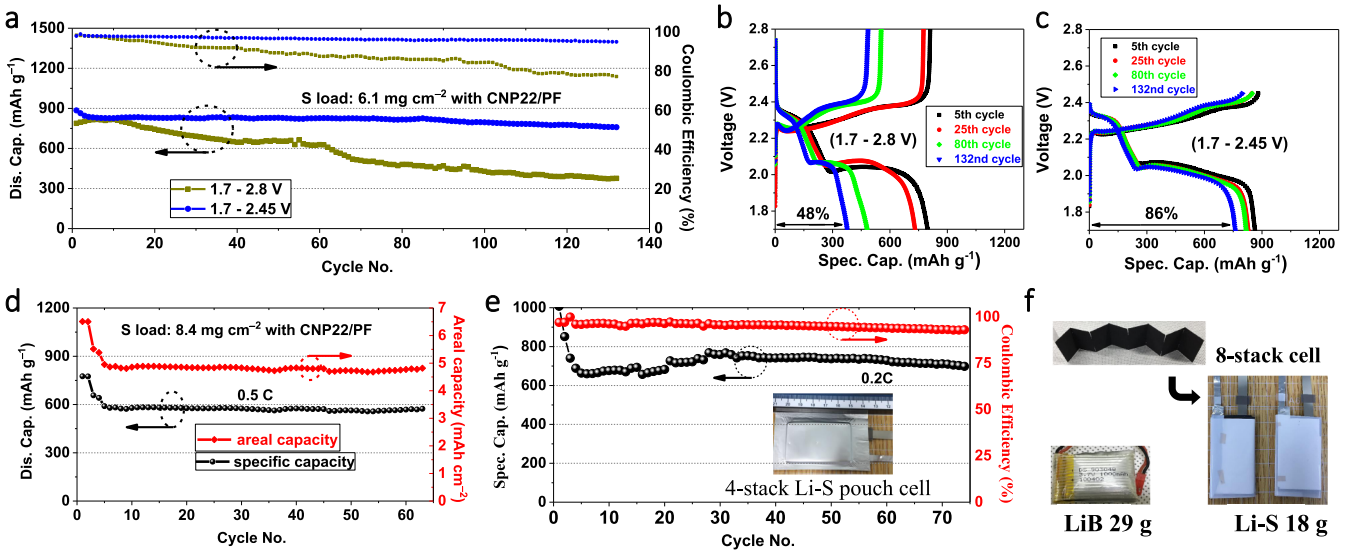

Figure 5. Reliable Li|CNP22/PF|S batteries. (a) Li−S cells at a high-S-loading of 6.1 mg cm^{-2} and CNP22/PF (at 0.5 C), with two charging cutoff voltages, i.e., 2.8 and 2.45 V. (b,c) Corresponding galvanostatic charge/discharge profiles of the Li−S cells operated in the range 1.7−2.8 and 1.7−2.45 V. (d) Discharge capacity and areal capacity of high-S-loaded (8.4 mg cm^{-2}) Li−S cell with CNP22/PF (at 0.5 C) and the voltage range 1.7−2.45 V. (e) Electrochemical performance of a 4-stack Li−S pouch cell (at 0.2 C) with the high-S-loading cathode of 6.1 mg cm^{-2}. The inset in (e) shows a digital photograph of the 4-stack Li−S pouch cell (3 × 5 cm^2). (f) Powering a minihelicopter by two Li−S pouch cells (8-stack in each pouch cell), which have estimated the capacity of 1400 mA h. The left inset shows a LiB provided by a manufacturer for a minihelicopter, and right inset shows two 8-stack pouch cells before packaging.

CNP22 effectively mitigates the migration of LiPS from the S cathode to the Li anode. It is known that the charge-transfer capability in a Li−S cell is directly proportional to the reaction kinetics, as reflected in the polarization of the voltage profiles.[55] The averaged polarizations obtained from the voltage profiles of the 288th cycle are calculated to be 327 and 265 mV for the Li|PF|S and Li|CNP22/PF|S cells, respectively (Figure 4c), which are in agreement with the CV analysis shown in Figure 3c. The lower polarization in Li|CNP22/PF|S cell means that there exists a greater number of active sites created by the presence of C, N, and P, which improves the affinity of CNP22 toward S and the conducting agents. This property enhances S utilization and maintains stable redox reactions between S and Li over long cycling.

3.5. Constructing Reliable Li|CNP22/PF|S Batteries. After confirmation of the high electrochemical performance, the construction of reliable Li|CNP22/PF|S batteries was performed for comparison with LiBs, especially in terms of volumetric and gravimetric energy densities. In practice, most cathodes designed for LiBs have an areal capacity greater than 4 mA h cm^{-2}. The S cathode was designed to contain more than 6 mg cm^{-2} of pure S to meet this minimum requirement and to ensure the superiority of the Li−S cell over the LiBs. However, the capacity of a Li−S cell with a high-S-loaded cathode drops sharply because of the physicochemical instability of the electrode.[56] The presence of concentrated LiPS in the electrolyte greatly decreases the stability of the Li anode.[57] More importantly, we assume that a high charging voltage may increase parasitic reactions on the Li anode surface. Therefore, the charging cutoff voltage for pragmatic cycling conditions needs to be carefully chosen and evaluated. The cycling performances of the Li|CNP22/PF|S cell at high-S-load (6.1 mg cm^{-2}) with various charging cutoff voltages are shown in Figure 5a. The CE values over 132 cycles are 77.4 and 95%, corresponding to cutoff voltages of 2.8 and 2.45 V (Figure 5a), respectively. For the cutoff voltage of 2.8 V, the cycling performance deteriorates, with a discharge capacity of 376.2 mA h g^{-1} after 132 cycles. Interestingly, the cutoff voltage of 2.45 V delivers a higher discharge capacity, that is, 759 mA h g^{-1}. The voltage profiles at the 5th, 25th, 80th, and 132nd cycles of the cell operated in the range 1.7−2.8 V showed a significant decrease in capacity (retention of 48%) after 132 cycles (Figure 5b). However, in the case of the cell operated in the range 1.7−2.45 V, the capacity retention is 86%, as seen in Figure 5c. This result implies that shuttling phenomenon may possibly be promoted by the faster oxidation of LiPS at high voltage. There is no significant effect on the charging capacity from 2.45 to 2.8 V, but this high-voltage range damages the electrodes because side reactions between the Li anode and the electrolyte, LiPS or salt may consume active materials and passivate the Li anode interface, as well as induce the formation and proliferation of Li dendrites.[16] When CNP22 is applied, the Li−S cell can be fully charged at a low cutoff voltage, that is, 2.45 V, which helps to alleviate shuttling and preserve the Li anode. We assume that the electrochemical interactions occur directly on the CNP22 substrate, as described above, and can allow the recharging process to be fully charged at 2.45 V. Lowering the charging voltage is therefore crucial for improving the cycling ability of the Li|CNP22/PF|S cell at a high-S-load. We reassert the above conclusion by testing the electrochemical performance of the Li|CNP22/PF|S cell at a higher S loading of 8.4 mg cm^{-2}, as shown in Figure 5d. The result shows that the cell capacity reaches 590 mA h g^{-1} (at 0.5 C) after 63 cycles, with an areal capacity of 4.95 mA h cm^{-2}; this capacity exceeds that of the LiBs. However, the above results are based on a coin-cell configuration, which might not directly translate to the performance of actual Li−S batteries, especially when the batteries are constructed with larger dimensions and multi-stacked configurations. We, therefore, fabricated multistacked pouch Li−S batteries and investigated their electrochemical performances for practical applications. Figure 5e shows the

DOI: 10.1021/acsami.8b22249
ACS Appl. Mater. Interfaces 2019, 11, 11431−11441

capacity of a 4-stack (size 3 × 5 cm^2) pouch cell with a S loading of 6.1 mg cm^{-2}, which ran steadily over 74 cycles at 0.2 C. A digital photograph of the 4-stack Li−S pouch cell after assembly is shown in the inset in Figure 5e. The results show that a capacity of 699 mA h g^{-1} and CE of 93% are obtained after 74 cycles. To the best of our knowledge, such a high-S-loaded multistack pouch cell has not been shown in previous studies. The excellent performance of such a pouch cell was further established by replacing the power supply of a minihelicopter, which was designed by the manufacturer for use with a 1000 mA h (LiB) battery (Figure 5f). Two Li−S pouch cells with 8-stack in each cell were assembled and connected in series with a minihelicopter (total estimated capacity 1400 mA h). Furthermore, the Li−S pouch cells (18 g) are substantially lighter than the LiBs (29 g). The advantages of the Li−S pouch cells with CNP22 are very clear; therefore, CNP22 is a suitable material for constructing reliable Li−S batteries.

4. CONCLUSIONS

We developed a strategy for effectively suppressing the shuttling phenomenon and reducing the degradation of the electrodes in Li−S systems by the incorporation of a superior LiPS adsorption material, that is, CNP22. The experimental results confirm that CNP22 is an amorphous material, and the DFT calculations show a narrowing of the band gap by the exchange of ∼22 atomic percentage of C by P. The DFT calculations also explained the mechanisms behind the formation of electrostatic Li−N and covalent S−P bonds between LiPS and CNP22, which play an important role in suppressing the LiPS shuttling and prolonging the cycling life of Li−S systems. Indeed, a Li|CNP22/PF|S cell shows a high capacity and low decay rate over 700 cycles; this is primarily ascribed to strong interactions between LiPS and CNP22, as well as a high S reutilization during cycling. The support of CNP22 in the Li−S cell delivered sufficient capacity at a charging cutoff voltage of 2.45 V, which minimized side reactions and enabled the high-performance Li−S systems. For cathodes with a high-S-load, CNP22 helps to maintain the high performance in both the coin cell and pouch cell. Therefore, we believe that the use of amorphous CNP22 will enable the production and scale-up of practical Li−S batteries.

ASSOCIATED CONTENT

Supporting Information

The Supporting Information is available free of charge on the ACS Publications website at DOI: 10.1021/acsami.8b22249.

Electrochemical performance test; material characterization; high-S-loaded cathode fabrication; computational details; optimization of P concentration in CNP; synthesis process of CNP; yield of urea/diammonium phosphate pyrolysis corresponding to CNP0 and CNP; STEM mapping images were measured at 119 K magnification; CNP22/PF coating process; thermal stability of the CNPx materials; molecular structures of various LiPS and S_8 molecule; adsorption of Li_2S_6 on CNP22 supercell; digital photographs of the S cathode and corresponding SEM images; XPS spectra; LiPS adsorption experiment; observation on LiPS adsorbability of CNP22 based on the color change; variation of energy and the external pressure with increase in the lattice constant of unit cell of CNP22; Bader charge analysis; volumetric energy density; gravimetric energy density; percentage of pure S in the S/C composite; and SEM and corresponding EDX measurements; optimization of P concentration in CNP (PDF)

AUTHOR INFORMATION

Corresponding Authors

*E-mail: krlee@kist.re.kr (K.R.L.).
*E-mail: wonic@kist.re.kr (W.I.C.).

ORCID

Won Il Cho: 0000-0003-3801-0020

Author Contributions

V.D.D. and Deepika contributed equally to this work. The manuscript was written through contributions of all authors. All authors have given approval to the final version of the manuscript.

Notes

The authors declare no competing financial interest.

ACKNOWLEDGMENTS

This work was supported by the Korea Institute of Science and Technology (KIST) Institutional Program (project no. 2E29650) and the National Research Foundation of Korea (NRF-2016M1B3A1A01937324 and NRF-2016M3A7B4025402). Deepika and K.R.L. thank virtual lab to get the Cloud Computing Interface and KIST supercomputing facility.

REFERENCES

(1) Wang, J.; Li, Y.; Sun, X. Challenges and opportunities of nanostructured materials for aprotic rechargeable lithium−air batteries. *Nano Energy* **2013**, *2*, 443−467.

(2) Berckmans, G.; Messagie, M.; Smekens, J.; Omar, N.; Vanhaverbeke, L.; Van Mierlo, J. Cost projection of state of the art lithium-ion batteries for electric vehicles up to 2030. *Energies* **2017**, *10*, 1314.

(3) Rehman, S.; Khan, K.; Zhao, Y.; Hou, Y. Nanostructured cathode materials for lithium−sulfur batteries: Progress, challenges and perspectives. *J. Mater. Chem. A* **2017**, *5*, 3014−3038.

(4) Fang, R.; Zhao, S.; Sun, Z.; Wang, D. W.; Cheng, H. M.; Li, F. More reliable lithium-sulfur batteries: Status, solutions and prospects. *Adv. Mater.* **2017**, *29*, 1606823.

(5) Kim, M. S.; Ryu, J.-H.; Deepika, Y. R.; Lim, Y. R.; Nah, I. W.; Lee, K.-R.; Archer, L. A. Langmuir-Blodgett artificial solid-electrolyte interphases for practical lithium metal batteries. *Nat. Energy* **2018**, *3*, 889.

(6) Yang, Z.; Ong, P. V.; He, Y.; Wang, L.; Bowden, M. E.; Xu, W.; Droubay, T. C.; Wang, C.; Sushko, P. V.; Du, Y. Direct visualization of li dendrite effect on licoo2 cathode by in situ tem. *Small* **2018**, *14*, 1803108.

(7) Deng, K.; Qin, J.; Wang, S.; Ren, S.; Han, D.; Xiao, M.; Meng, Y. Effective suppression of lithium dendrite growth using a flexible single-ion conducting polymer electrolyte. *Small* **2018**, *14*, 1801420.

(8) Cheng, X.-B.; Peng, H.-J.; Huang, J.-Q.; Wei, F.; Zhang, Q. Dendrite-free nanostructured anode: Entrapment of lithium in a 3d fibrous matrix for ultra-stable lithium−sulfur batteries. *Small* **2014**, *10*, 4257−4263.

(9) Chai, J.; Chen, B.; Xian, F.; Wang, P.; Du, H.; Zhang, J.; Liu, Z.; Zhang, H.; Dong, S.; Zhou, X. Dendrite-free lithium deposition via flexible-rigid coupling composite network for lini0. 5mn1. 5o4/li metal batteries. *Small* **2018**, *14*, 1802244.

(10) Farooqi, S. A.; Wang, X.; Lu, H.; Li, Q.; Tang, K.; Chen, Y.; Yan, C. Single-nanostructured electrochemical detection for intrinsic mechanism of energy storage: Progress and prospect. *Small* **2018**, *14*, 1803482.

DOI: 10.1021/acsami.8b22249
ACS Appl. Mater. Interfaces 2019, 11, 11431−11441

(11) Zhu, Y.; Wang, S.; Miao, Z.; Liu, Y.; Chou, S. L. Novel non-carbon sulfur hosts based on strong chemisorption for lithium−sulfur batteries. *Small* **2018**, *14*, 1801987.
(12) Fang, X.; Peng, H. A Revolution in Electrodes: Recent Progress in Rechargeable Lithium-Sulfur Batteries. *Small* **2015**, *11*, 1488−1511.
(13) Kong, L.-L.; Zhang, Z.; Zhang, Y.-Z.; Liu, S.; Li, G.-R.; Gao, X.-P. Porous Carbon Paper as Interlayer to Stabilize the Lithium Anode for Lithium-Sulfur Battery. *ACS Appl. Mater. Interfaces* **2016**, *8*, 31684−31694.
(14) Ma, L.; Kim, M. S.; Archer, L. A. Stable artificial solid electrolyte interphases for lithium batteries. *Chem. Mater.* **2017**, *29*, 4181−4189.
(15) Kozen, A. C.; Lin, C.-F.; Zhao, O.; Lee, S. B.; Rubloff, G. W.; Noked, M. Stabilization of lithium metal anodes by hybrid artificial solid electrolyte interphase. *Chem. Mater.* **2017**, *29*, 6298−6307.
(16) Liu, J.; Lu, D.; Zheng, J.; Yan, P.; Wang, B.; Sun, X.; Shao, Y.; Wang, C.; Xiao, J.; Zhang, J.-G. Minimizing polysulfide shuttle effect in lithium-ion sulfur batteries by anode surface passivation. *ACS Appl. Mater. Interfaces* **2018**, *10*, 21965−21972.
(17) Dong, Q.; Shen, R.; Li, C.; Gan, R.; Ma, X.; Wang, J.; Li, J.; Wei, Z. Construction of soft base tongs on separator to grasp polysulfides from shuttling in lithium−sulfur batteries. *Small* **2018**, *14*, 1804277.
(18) Kim, M. S.; Kim, M.-S.; Do, V.; Lim, Y. R.; Nah, I. W.; Archer, L. A.; Cho, W. I. Designing solid-electrolyte interphases for lithium sulfur electrodes using ionic shields. *Nano Energy* **2017**, *41*, 573−582.
(19) Hoang, V. C.; Do, V.; Nah, I. W.; Lee, C.; Cho, W. I.; Oh, I. H. Facile coating of graphene interlayer onto li2s as a high electrochemical performance cathode for lithium sulfur battery. *Electrochim. Acta* **2016**, *210*, 1−6.
(20) Chiochan, P.; Kaewruang, S.; Phattharasupakun, N.; Wutthiprom, J.; Maihom, T.; Limtrakul, J.; Nagarkar, S.; Horike, S.; Sawangphruk, M. Chemical Adsorption and Physical Confinement of Polysulfides with the Janus-faced Interlayer for High-performance Lithium-Sulfur Batteries. *Sci. Rep.* **2017**, *7*, 17703.
(21) Qu, H.; Zhang, J.; Du, A.; Chen, B.; Chai, J.; Xue, N.; Wang, L.; Qiao, L.; Wang, C.; Zang, X. Multifunctional sandwich-structured electrolyte for high-performance lithium−sulfur batteries. *Adv. Sci.* **2018**, *5*, 1700503.
(22) Singhal, R.; Chung, S.-H.; Manthiram, A.; Kalra, V. A free-standing carbon nanofiber interlayer for high-performance lithium−sulfur batteries. *J. Mater. Chem. A* **2015**, *3*, 4530−4538.
(23) Chung, S.-H.; Manthiram, A. Designing Lithium-Sulfur Batteries with High-Loading Cathodes at a Lean Electrolyte Condition. *ACS Appl. Mater. Interfaces* **2018**, *10*, 43749−43759.
(24) Li, Y.; Cai, Q.; Wang, L.; Li, Q.; Peng, X.; Gao, B.; Huo, K.; Chu, P. K. Mesoporous TiO2 Nanocrystals/Graphene as an Efficient Sulfur Host Material for High-Performance Lithium-Sulfur Batteries. *ACS Appl. Mater. Interfaces* **2016**, *8*, 23784−23792.
(25) Zhang, L.; Chen, X.; Wan, F.; Niu, Z.; Wang, Y.; Zhang, Q.; Chen, J. Enhanced electrochemical kinetics and polysulfide traps of indium nitride for highly stable lithium−sulfur batteries. *ACS Nano* **2018**, *12*, 9578−9586.
(26) Li, X.; Lu, Y.; Hou, Z.; Zhang, W.; Zhu, Y.; Qian, Y.; Liang, J.; Qian, Y. Sns2-compared to sno2-stabilized s/c composites toward high-performance lithium sulfur batteries. *ACS Appl. Mater. Interfaces* **2016**, *8*, 19550−19557.
(27) Guo, B.; Bandaru, S.; Dai, C.; Chen, H.; Zhang, Y.; Xu, Q.; Bao, S.; Chen, M.; Xu, M. Self-Supported FeCo2S4 Nanotube Arrays as Binder-Free Cathodes for Lithium-Sulfur Batteries. *ACS Appl. Mater. Interfaces* **2018**, *10*, 43707−43715.
(28) Yang, Y.; Zhang, L.; Xu, H.; Qin, X.; Deng, Y.; Chen, G. Net-structured filter of co (oh) 2-anchored carbon nanofibers with ketjen black for high performance li−s batteries. *ACS Sustainable Chem. Eng.* **2018**, *6*, 17099−17107.
(29) Liu, Y.; Qin, X.; Zhang, S.; Liang, G.; Kang, F.; Chen, G.; Li, B. Fe3o4-decorated porous graphene interlayer for high-performance lithium−sulfur batteries. *ACS Appl. Mater. Interfaces* **2018**, *10*, 26264−26273.
(30) Luo, L.; Qin, X.; Wu, J.; Liang, G.; Li, Q.; Liu, M.; Kang, F.; Chen, G.; Li, B. An interwoven moo 3@ cnt scaffold interlayer for high-performance lithium−sulfur batteries. *J. Mater. Chem. A* **2018**, *6*, 8612−8619.
(31) Song, J.; Gordin, M. L.; Xu, T.; Chen, S.; Yu, Z.; Sohn, H.; Lu, J.; Ren, Y.; Duan, Y.; Wang, D. Strong lithium polysulfide chemisorption on electroactive sites of nitrogen-doped carbon composites for high-performance lithium−sulfur battery cathodes. *Angew. Chem.* **2015**, *127*, 4399−4403.
(32) Gulzar, U.; Li, T.; Bai, X.; Colombo, M.; Ansaldo, A.; Marras, S.; Prato, M.; Goriparti, S.; Capiglia, C.; Proietti Zaccaria, R. Nitrogen-doped single-walled carbon nanohorns as a cost-effective carbon host toward high-performance lithium−sulfur batteries. *ACS Appl. Mater. Interfaces* **2018**, *10*, 5551−5559.
(33) He, F.; Li, K.; Yin, C.; Ding, Y.; Tang, H.; Wang, Y.; Wu, Z. A combined theoretical and experimental study on the oxygenated graphitic carbon nitride as a promising sulfur host for lithium−sulfur batteries. *J. Power Sources* **2018**, *373*, 31−39.
(34) Wang, J.; Meng, Z.; Yang, W.; Yan, X.; Guo, R.; Han, W.-Q. Facile synthesis of rgo/g-c3n4/cnt microspheres via ethanol-assisted spray drying method for high performance lithium-sulfur batteries. *ACS Appl. Mater. Interfaces* **2018**, *11*, 819−827.
(35) Yao, S.; Xue, S.; Peng, S.; Jing, M.; Qian, X.; Shen, X.; Li, T.; Wang, Y. Synthesis of graphitic carbon nitride at different thermal-pyrolysis temperature of urea and it application in lithium−sulfur batteries. *J. Mater. Sci.: Mater. Electron.* **2018**, *29*, 17921−17930.
(36) Qu, L.; Liu, P.; Yi, Y.; Wang, T.; Yang, P.; Tian, X.; Li, M.; Yang, B.; Dai, S. Enhanced cycling performance for lithium−sulfur batteries by a laminated 2d g-c3n4/graphene cathode interlayer. *ChemSusChem* **2019**, *12*, 213.
(37) Song, X.; Zhang, M.; Yao, M.; Hao, C.; Qiu, J. A new insight into the anchoring mechanism of polysulfides inside nanoporous covalent organic frameworks for lithium-sulfur batteries. *ACS Appl. Mater. Interfaces* **2018**, *10*, 43896.
(38) Zhang, Y.; Mori, T.; Ye, J.; Antonietti, M. Phosphorus-doped carbon nitride solid: Enhanced electrical conductivity and photocurrent generation. *J. Am. Chem. Soc.* **2010**, *132*, 6294−6295.
(39) Zhang, L.; Chen, X.; Guan, J.; Jiang, Y.; Hou, T.; Mu, X. Facile synthesis of phosphorus doped graphitic carbon nitride polymers with enhanced visible-light photocatalytic activity. *Mater. Res. Bull.* **2013**, *48*, 3485−3491.
(40) Kresse, G.; Hafner, J. Norm-conserving and ultrasoft pseudopotentials for first-row and transition elements. *J. Phys.: Condens. Matter* **1994**, *6*, 8245.
(41) Jiang, J.; Ou-yang, L.; Zhu, L.; Zheng, A.; Zou, J.; Yi, X.; Tang, H. Dependence of electronic structure of g-C 3 N 4 on the layer number of its nanosheets: A study by Raman spectroscopy coupled with first-principles calculations. *Carbon* **2014**, *80*, 213−221.
(42) Dai, H.; Gao, X.; Liu, E.; Yang, Y.; Hou, W.; Kang, L.; Fan, J.; Hu, X. Synthesis and characterization of graphitic carbon nitride sub-microspheres using microwave method under mild condition. *Diamond Relat. Mater.* **2013**, *38*, 109−117.
(43) Kang, Y.; Yang, Y.; Yin, L.-C.; Kang, X.; Liu, G.; Cheng, H.-M. An Amorphous Carbon Nitride Photocatalyst with Greatly Extended Visible-Light-Responsive Range for Photocatalytic Hydrogen Generation. *Adv. Mater.* **2015**, *27*, 4572−4577.
(44) Zhang, Q.; Wang, Y.; Seh, Z. W.; Fu, Z.; Zhang, R.; Cui, Y. Understanding the anchoring effect of two-dimensional layered materials for lithium−sulfur batteries. *Nano Lett.* **2015**, *15*, 3780−3786.
(45) Van Santen, R. A.; Tranca, I. How molecular is the chemisorptive bond? *Phys. Chem. Chem. Phys.* **2016**, *18*, 20868−20894.
(46) Wang, Y.; Zhang, B.; Xu, M.; He, X. Tunable Ternary (p, sn)-doped graphene as an efficient electrocatalyst for oxygen reduction reaction in an alkaline medium. *RSC Adv.* **2015**, *5*, 86746−86753.

DOI: 10.1021/acsami.8b22249
ACS Appl. Mater. Interfaces 2019, 11, 11431−11441

(47) Fan, C.-Y.; Yuan, H.-Y.; Li, H.-H.; Wang, H.-F.; Li, W.-L.; Sun, H.-Z.; Wu, X.-L.; Zhang, J.-P. The effective design of a polysulfide-trapped separator at the molecular level for high energy density li−s batteries. *ACS Appl. Mater. Interfaces* **2016**, *8*, 16108−16115.
(48) Fantauzzi, M.; Elsener, B.; Atzei, D.; Rigoldi, A.; Rossi, A. Exploiting xps for the identification of sulfides and polysulfides. *RSC Adv.* **2015**, *5*, 75953−75963.
(49) Murata, K.; Ikeda, S.; Utsunomiya, T.; Yasui, A. X-ray photoelectron spectrometric and x-ray fluorometric studies of sulphur compounds on the surface of copper plates exposed to the atmosphere. *Talanta* **1976**, *23*, 529−533.
(50) Choudhury, D.; Das, B.; Sarma, D. D.; Rao, C. N. R. Xps evidence for molecular charge-transfer doping of graphene. *Chem. Phys. Lett.* **2010**, *497*, 66−69.
(51) Huang, J.-Q.; Zhang, Q.; Peng, H.-J.; Liu, X.-Y.; Qian, W.-Z.; Wei, F. Ionic shield for polysulfides towards highly-stable lithium−sulfur batteries. *Energy Environ. Sci.* **2014**, *7*, 347−353.
(52) Lu, Y.; Li, X.; Liang, J.; Hu, L.; Zhu, Y.; Qian, Y. A simple melting-diffusing-reacting strategy to fabricate s/nis 2−c for lithium−sulfur batteries. *Nanoscale* **2016**, *8*, 17616−17622.
(53) Barchasz, C.; Molton, F.; Duboc, C.; Leprêtre, J.-C.; Patoux, S. b.; Alloin, F. Lithium/sulfur cell discharge mechanism: An original approach for intermediate species identification. *Anal. Chem.* **2012**, *84*, 3973−3980.
(54) Knap, V.; Stroe, D.-I.; Swierczynski, M.; Teodorescu, R.; Schaltz, E. Investigation of the self-discharge behavior of lithium-sulfur batteries. *J. Electrochem. Soc.* **2016**, *163*, A911−A916.
(55) Chung, S.-H.; Manthiram, A. Designing lithium-sulfur cells with practically necessary parameters. *Joule* **2018**, *2*, 710−724.
(56) Peng, H.-J.; Huang, J.-Q.; Cheng, X.-B.; Zhang, Q. Review on High-Loading and High-Energy Lithium-Sulfur Batteries. *Adv. Energy Mater.* **2017**, *7*, 1700260.
(57) Yan, C.; Cheng, X.-B.; Zhao, C.-Z.; Huang, J.-Q.; Yang, S.-T.; Zhang, Q. Lithium metal protection through in-situ formed solid electrolyte interphase in lithium-sulfur batteries: The role of polysulfides on lithium anode. *J. Power Sources* **2016**, *327*, 212−220.

DOI: 10.1021/acsami.8b22249
ACS Appl. Mater. Interfaces 2019, 11, 11431−11441